

Electronic thermal transport measurement in low-dimensional materials with graphene non-local noise thermometry

Jonah Waissman¹, Laurel E. Anderson¹, Artem V. Talanov^{1,2}, Zhongying Yan¹, Young J. Shin¹, Danial H. Najafabadi¹, Mehdi Rezaee², Xiaowen Feng³, Daniel G. Nocera³, Takashi Taniguchi⁴, Kenji Watanabe⁵, Brian Skinner⁶, Konstantin A. Matveev⁷ and Philip Kim^{1,2}

In low-dimensional systems, the combination of reduced dimensionality, strong interactions and topology has led to a growing number of many-body quantum phenomena. Thermal transport, which is sensitive to all energy-carrying degrees of freedom, provides a discriminating probe of emergent excitations in quantum materials and devices. However, thermal transport measurements in low dimensions are dominated by the phonon contribution of the lattice, requiring an experimental approach to isolate the electronic thermal conductance. Here we measured non-local voltage fluctuations in a multi-terminal device to reveal the electronic heat transported across a mesoscopic bridge made of low-dimensional materials. Using two-dimensional graphene as a noise thermometer, we measured the quantitative electronic thermal conductance of graphene and carbon nanotubes up to 70 K, achieving a precision of ~1% of the thermal conductance quantum at 5 K. Employing linear and nonlinear thermal transport, we observed signatures of energy transport mediated by long-range interactions in one-dimensional electron systems, in agreement with a theoretical model.

eat transport by electrons has been central to the study of materials ever since the pivotal measurements of Wiedemann and Franz¹. For weakly interacting electronic systems such as normal metals, the ground state is described by Landau's Fermi liquid paradigm, and electronic charge and heat flow are intimately connected, giving rise to the Wiedemann–Franz (WF) law. If interactions are sufficiently strong, weakly interacting charged quasiparticles no longer describe system behaviour and the WF law breaks down. Notable examples of such strongly interacting systems include quasi-one-dimensional materials², metallic ferromagnets³, heavy fermion materials⁴, underdoped cuprates⁵ and the charge-neutral point of graphene⁶, all cases related to the emergence of non-Fermi liquid behaviour due to strong interactions.

In low-dimensional systems, such as two-dimensional (2D) quantum materials and one-dimensional (1D) nanowires, these electronic interaction effects (including spin) are enhanced. A growing number of strongly correlated states involving interactions and topology have been identified, including 1D and 2D electron Wigner crystals^{7–9}, strongly correlated insulators and superconductors in twisted 2D heterostructures¹⁰, and 2D magnets¹¹. Thermal transport experiments are of immediate interest to clarify the nature of these materials¹². Furthermore, the growing technological relevance of 1D and 2D materials demands an experimental probe of electronic energy transport and dissipation properties, separated from other degrees of freedom.

Accessing electronic thermal transport is challenging due to the prevailing phonon contribution¹³. In bulk materials, the electronic contribution can be extracted by extrapolation to the low temperature

limit where the phonon contribution rapidly decays⁵, by using a magnetic field to separate the electronic contribution with the thermal Hall effect² or by chemical doping to re-enter the WF regime and thereby estimate the phonon contribution in an isostructural sample⁴. Electronic thermal transport has also been successfully isolated in some mesoscopic systems, notably quantum Hall systems^{14–17}, single-electron transistors¹⁸ and atomic contacts^{19,20}, by implementing electronic thermometry specific to the system of study^{6,21–24}. However, for low-dimensional materials, such as 2D van der Waals monolayers²⁵ and 1D nanotubes²⁶ and molecular junctions^{27,28}, existing techniques are dominated by phonon transport and a method that quantitatively isolates the electronic contribution is yet to be realized.

Multi-terminal noise and non-local thermometry

We approached this problem using Johnson–Nyquist noise, the fluctuations of voltage or current arising due to the finite temperature of electrical conductors^{29,30}. Classically, the voltage fluctuations of a resistor are given by

$$\langle V^2 \rangle = 4k_{\rm B}TR\Delta f$$

where $k_{\rm B}$ is the Boltzmann constant, T is the temperature, R is the electrical resistance and Δf is the measurement frequency bandwidth. Johnson–Nyquist noise is independent of the material type, size or shape, operating over a wide frequency band and temperature range, and is thus widely used in fundamental science and applications³¹. In two-terminal mesoscale samples, Johnson–Nyquist

¹Department of Physics, Harvard University, Cambridge, MA, USA. ²John A. Paulson School of Engineering and Applied Sciences, Harvard University, Cambridge, MA, USA. ³Department of Chemistry and Chemical Biology, Harvard University, Cambridge, MA, USA. ⁴International Center for Materials Nanoarchitectonics, National Institute for Materials Science, Tsukuba, Japan. ⁵Research Center for Functional Materials, National Institute for Materials Science, Tsukuba, Japan. ⁶Department of Physics, The Ohio State University, Columbus, OH, USA. ⁷Materials Science Division, Argonne National Laboratory, Argonne, IL, USA. [∞]e-mail: pkim@physics.harvard.edu

ARTICLES

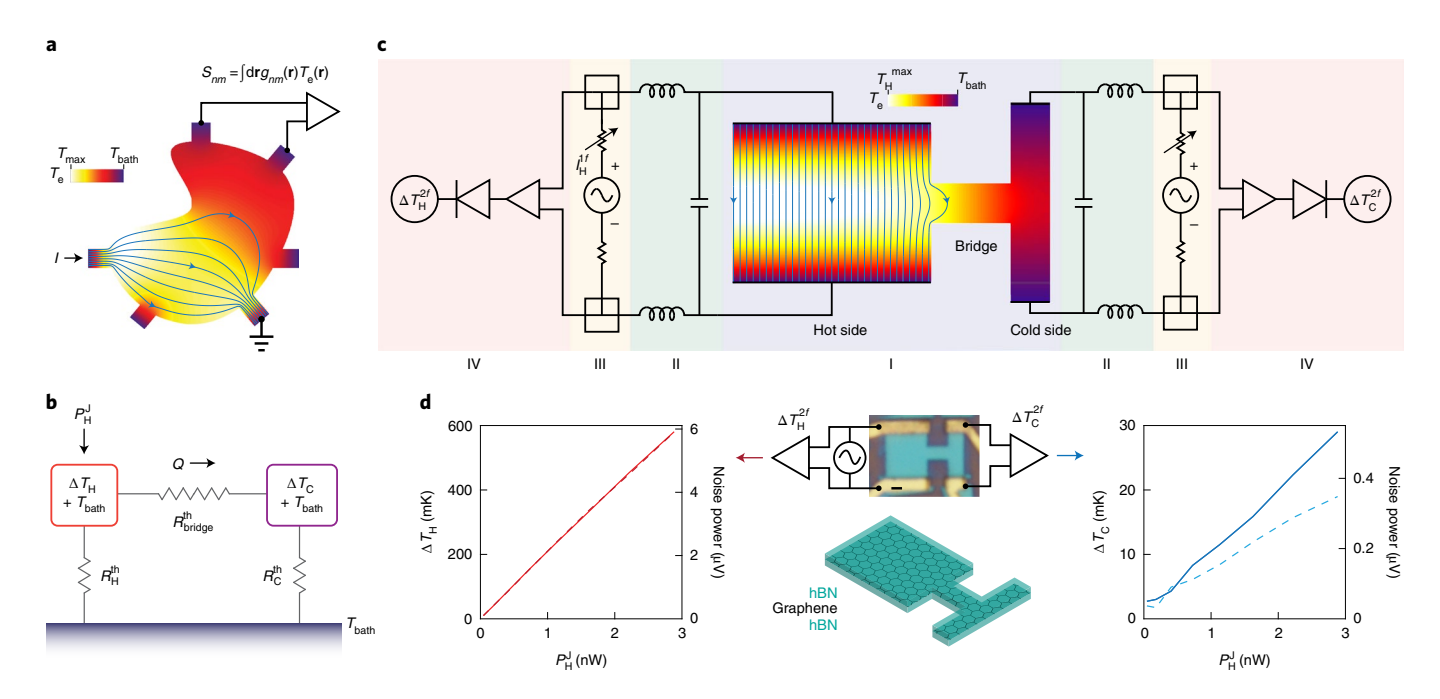


Fig. 1 | Nonlocal noise thermometry in multi-terminal devices. a, Schematic of multi-terminal noise measurement. A diffusive, conducting electron system is connected to terminals held at a bath temperature T_{bath}. Current is injected into one terminal and escapes through a ground, while other terminals are floating. Finite-element simulation of the temperature and current distribution assuming a uniform conductivity is shown in the colour scale and streamlines, respectively. In the absence of energy loss to phonons, the noise S_{nm} measured at any two terminals is given by a weighted function of the electronic temperature distribution $T_{e}(\mathbf{r})$ (see main text). **b**, Thermal circuit for a thermal conductance measurement. Joule power P_{H}^{l} is injected into a hot side reservoir connected by thermal resistance R_H^{th} to T_{bath} . The bridge thermal resistance R_{bridge}^{th} allows thermal current Q to cross from the hot to the cold side, connected to the bath by Rth. c, Circuit and geometry for non-local noise thermometry. Box I (blue, centre) shows a finite-element simulation of the device geometry. Joule power is dissipated on the hot side (left, wide rectangle) due to injected current density (streamlines). Thermal current is transported across the bridge while the electrical current across the bridge I_{bridge} is zero, causing heating of the cold side (right, narrow rectangle). Box II (green), box III (yellow) and box IV (red) correspond respectively to the balanced matching circuit, the balanced current excitation and resistance measurement, and the noise measurement amplification chain (see Methods for details). d, The upper image of the centre panel shows an optical image of the device (shown before top gate deposition for clarity). Scale bar, 1µm. A simplified schematic of the measurement set-up shown in c is overlaid on the optical image, showing the hot side current excitation and hot/cold side noise measurement. The lower image shows a device stack consisting of graphene encapsulated in hBN layers. The left (right) graph displays the hot (cold) side noise power and calibrated temperature change $\Delta T_{\rm H}$ ($\Delta T_{\rm C}$) versus the applied Joule power, $P_{L\nu}^{J}$ at $T_{bath} = 4.8$ K and fixed hot and cold side gate voltages at two values of bridge electron density (solid and dashed lines, corresponding to -8.0×10^{11} cm⁻² and -1.6×10^{11} cm⁻², respectively). On the hot side (left), $\Delta T_{\rm H}$ shows nearly identical rises for the two density values, owing to a small amount of power escaping across the bridge, whereas ΔT_{C} , which is far smaller, strongly depends on the bridge electron density, evidencing a difference in thermal current across the bridge.

noise can be used to measure electronic thermal conductance using self-heating^{21,22,32,33}, in which Joule power dissipated in a resistor is balanced by energy loss channels, generating a measurable temperature rise. Recently, this approach was used for graphene^{21,22,32,33}, in which electronic diffusion cooling governs energy loss over a wide temperature range, allowing electronic thermal conductance to be measured to $T > 100 \,\mathrm{K}$. However, because the device under test is simultaneously the thermometer, this approach is limited to diffusive conducting states with low energy loss to phonons and low contact resistance, restricting its use to graphene. A thermal transport measurement that applies to other materials and non-diffusive conduction requires a minimum of two temperature inputs to specify the temperature gradient driving energy flow. We thus require a multi-terminal approach, in which the local temperatures of two points along a device are measured by the fluctuations of the corresponding local resistors.

The multi-terminal generalization of Johnson–Nyquist noise can be found by considering the noise in diffusive multi-terminal conductors. An example is shown in Fig. 1a. A conducting system is connected to multiple leads held at a bath temperature. The leads may be grounded or floating. Current is injected through one of these leads, causing Joule heating of the system. In the limit that

electrons generate a local temperature through strong equilibration, known as the hot electron regime, it has been theoretically shown³⁴ that the noise power measured between any two terminals n and m is given by $S_{nm} = \int_{-\infty}^{\infty} dt \langle \delta I_n(t) \delta I_m(t) \rangle = \int d\mathbf{r} \mathbf{g}_{nm}(\mathbf{r}) \mathbf{T}_e(\mathbf{r})$. Here, t is time, δI_n and δI_m are the fluctuation currents, \mathbf{r} is a location in the conductor, $T_e(\mathbf{r})$ is the local electronic temperature and $g_{nm}(\mathbf{r})$ is a geometry-dependent local weighting function defined as

$$g_{nm}\left(\mathbf{r}\right) = \nabla\phi_n \cdot \hat{\sigma}\nabla\phi_m$$

where $\hat{\sigma}$ is the local conductivity and ϕ_n and ϕ_m are characteristic potentials associated with each terminal of the device (see Supplementary Section 4 for further details). This relationship holds if the energy supplied by Joule heating remains in the electronic degrees of freedom and energy losses to phonons and other heat sinks are negligible. Under these conditions, the noise emitted at any terminal is closely related to the energy transported to that region of the device and the resulting electronic temperature distribution.

For thermal conductance measurement, we sought to realize the thermal circuit sketched in Fig. 1b, in which two measured temperatures, the hot side temperature $T_{\rm H} = T_{\rm bath} + \Delta T_{\rm H}$, where $T_{\rm bath}$ is the

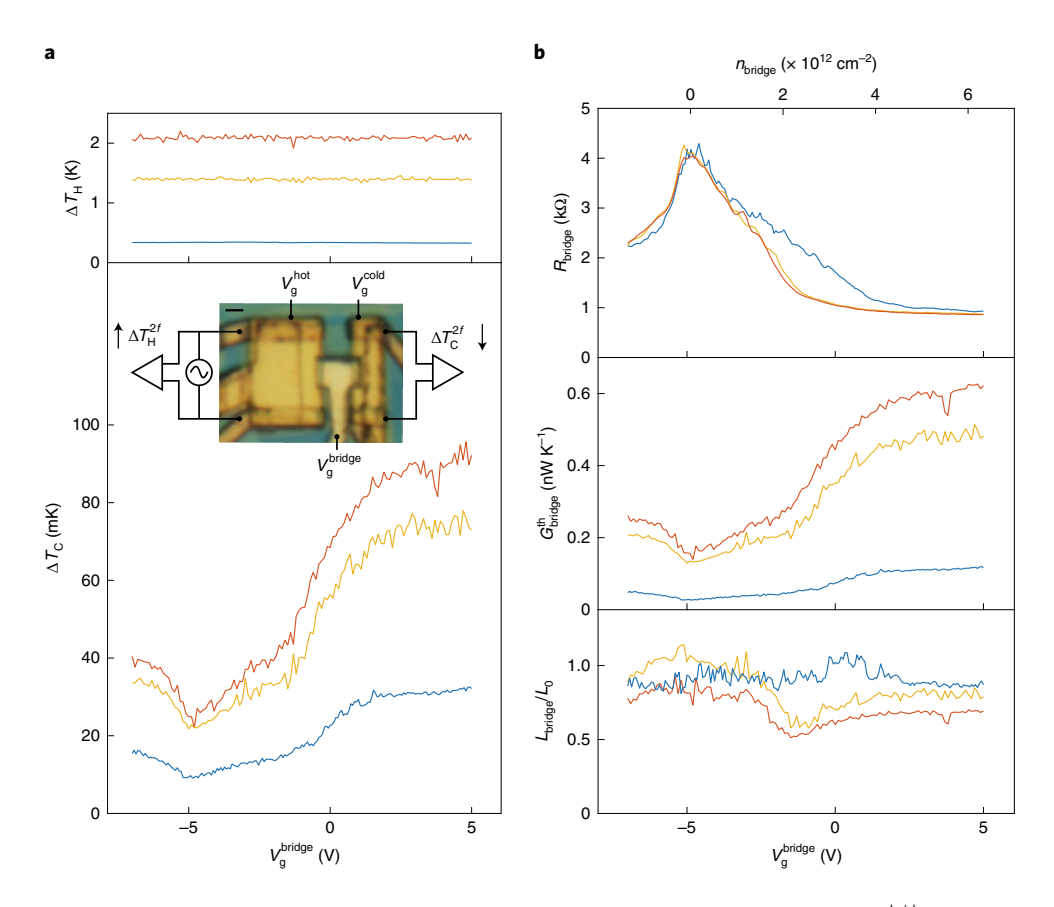


Fig. 2 | Electronic thermal conductance of graphene. a, Hot side temperature change $\Delta T_{\rm H}$ versus bridge gate voltage $V_{\rm g}^{\rm bridge}$ at fixed hot and cold side gate voltages $V_{\rm g}^{\rm bridge}$ (top). Corresponding cold side temperature change $\Delta T_{\rm C}$ versus bridge gate voltage $V_{\rm g}^{\rm bridge}$ (bottom). $T_{\rm bath} = 5$ K (blue), 20 K (yellow) and 30 K (red); this colour code applies to all graphs in **b**. The inset shows the optical image of the hBN-encapsulated graphene device after top gate deposition, overlaid on a schematic circuit diagram. Scale bar, 1μm. Current is injected into the hot side at frequency f, and the resulting modulated noise power on the hot and cold sides is measured to yield the temperature changes $\Delta T_{\rm H}^{\rm 2f}$ and $\Delta T_{\rm C}^{\rm 2f}$. **b**, Four-point electrical resistance of the bridge, $R_{\rm bridge}$ (bottom axis) and bridge carrier density $n_{\rm bridge}$ (top axis) at $T_{\rm bath} = 5$, 20 and 30 K (top graph). In this temperature range, the resistance is nearly temperature-independent. An excess resistance near $V_{\rm g}^{\rm bridge} = 0$ at the lowest measured temperature arises due to induced disorder of the atomic layer-deposited insulating layer beneath the top gates. Thermal conductance of the bridge $G_{\rm bridge}^{\rm th}$, deduced from the temperature changes and the independently measured cold side thermal conductance (see main text), versus $V_{\rm g}^{\rm bridge}$ at $T_{\rm bath} = 5$, 20 and 30 K (middle). Lorenz ratio of the bridge, $L_{\rm bridge}/L_{\rm o}$, versus $V_{\rm g}^{\rm bridge}$ at $T_{\rm bath} = 5$, 20 and 30 K (see main text for definition and discussion; bottom).

bath temperature and $\Delta T_{\rm H}$ is the hot side temperature change upon Joule heating, and the cold side temperature $T_{\rm C} = T_{\rm bath} + \Delta T_{\rm C}$, are combined with the energy current Q across a bridge between two thermometers to give the two-terminal thermal conductance $G_{\text{bridge}}^{\text{th}} = \frac{Q}{T_{\text{H}} - T_{\text{C}}}$. To accomplish this with multi-terminal noise, we used the geometry shown in the central panel of Fig. 1c. The device possesses four terminals divided into two pairs. Each pair contacts a rectangular conducting region, defining two diffusive electronic thermometers. A bridge connects the two rectangular thermometers at their midpoints and serves as the material of interest, which need not be diffusive. The wider rectangle on the left serves as the hot side, where diffusive electrons are Joule-heated by an injected low-frequency current. To avoid directly Joule-heating the bridge and cold side, the heating circuit is balanced such that only energy current Q and no electrical current traverses the bridge (see Supplementary Section 2 for details). The bridge width is narrow compared with the length of the hot side such that it obtains a thermal bias at the peak of the hot side temperature distribution. The narrow right-most rectangle serves as the cold side. Energy current across the bridge heats the cold side at its centre point and is equilibrated at the cold contacts, generating a peaked temperature distribution and non-local voltage fluctuations. The narrow cold side design optimizes sensitivity by maintaining a maximal average,

whereas the wide hot side ensures a local temperature distribution that is insensitive to the bridge. This geometry can be generalized to multi-thermometer set-ups such as for thermal Hall measurement by appending two-terminal thermometers at other points along the bridge (Supplementary Section 9).

Each thermometer should measure the local temperatures $T_{\rm H}$ and T_C without cross-contamination of signals, despite being in electrical contact. In a two-terminal rectangular geometry with uniform conductivity, the local weighting function $g_{nm}(\mathbf{r})$ is well-approximated to a constant and S_{nm} is proportional to the average $T_e(\mathbf{r})$. To maintain this constant weighting in the multi-terminal case, we defined a differential noise correlator $S_{n-m,n-m}$ for which the contribution from the bridge cancels and the measured noise is proportional to the temperature average on either side: $S_{\rm H} \propto \int {
m d}{f r} T_{\rm e} \left({f r}\right)$ and likewise for the cold side (see Supplementary Section 4.1 for a detailed discussion). We achieved this by implementing differential noise thermometry³⁵, in which differential thermal noise is amplified, bandpass-filtered and frequency-integrated, resulting in a voltage signal proportional to the total noise power in a frequency band, with non-overlapping bands chosen for the hot and cold sides (Fig. 1c, Methods and Supplementary Section 10). The geometry and circuit together allow for the isolation of the heat transport-induced non-local noise (Supplementary Section 4.1). To achieve an

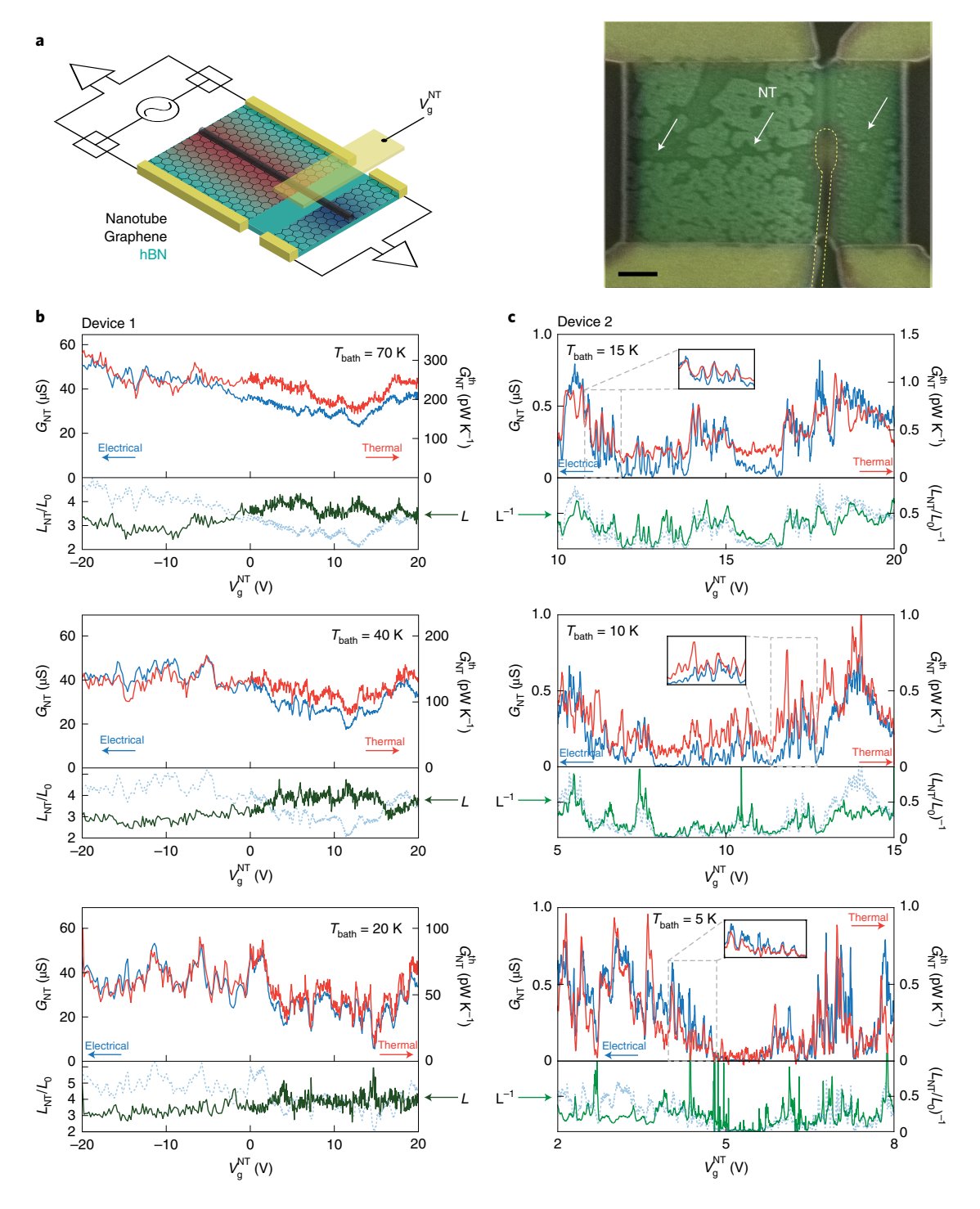


Fig. 3 | Electronic thermal conductance of carbon NTs. a, Schematic of the device in which two graphene thermometers are bridged by a carbon NT (left). A bottom hBN layer supports monolayer graphene, with an etched gap. A carbon NT connects the two graphene patches, which form the two noise thermometers. A local metallic top gate tunes the NT carrier density. Composite optical and scanning electron microscopy image of the device (right). Scale bar, 1μm. The dashed yellow line shows the location of the metal top gate. White arrows indicate the location of the NT, visible as a dark line in the composite image. **b**, Two-point electrical and thermal conductance of a small-bandgap NT in Device 1 at different temperatures (top panels). The corresponding Lorenz ratio $L_{\rm NT}/L_0$ is shown (dark green) in the lower panels, together with the electrical conductance shown in the respective upper panel (dotted light blue) to allow explicit comparison with $L_{\rm NT}/L_0$. All thermal quantities are lower bounds (see main text and Supplementary Section 7). The thermal bias for all plots is $\Delta T_{\rm Pl}/T_{\rm bath} = 0.1$. See Supplementary Section 12 for the data for $T_{\rm bath} = 5$ K. **c**, Two-point electrical and thermal conductance measured in Device 2 with a high-resistance NT bridge at different temperatures (top panels). The corresponding inverse Lorenz ratio $(L_{\rm NT}/L_0)^{-1}$ is shown (green) in the lower panels, together with the electrical conductance reproduced from the respective upper panel (dotted light blue). Top and middle panels, $\Delta T_{\rm Pl}/T_{\rm bath} = 1$; bottom panel, $\Delta T_{\rm Pl}/T_{\rm bath} = 0.5$. A d.c. voltage of 30 mV was applied across the NT to overcome the contact barrier; the corresponding measured d.c. current on the nanoampere scale led to negligible background heating and did not affect the measurements at the 2f heating frequency. All NT thermal quantities are lower bounds (see main text and Supplementary Section 7). The insets show magnifications of Coulomb peaks. See Supplementary

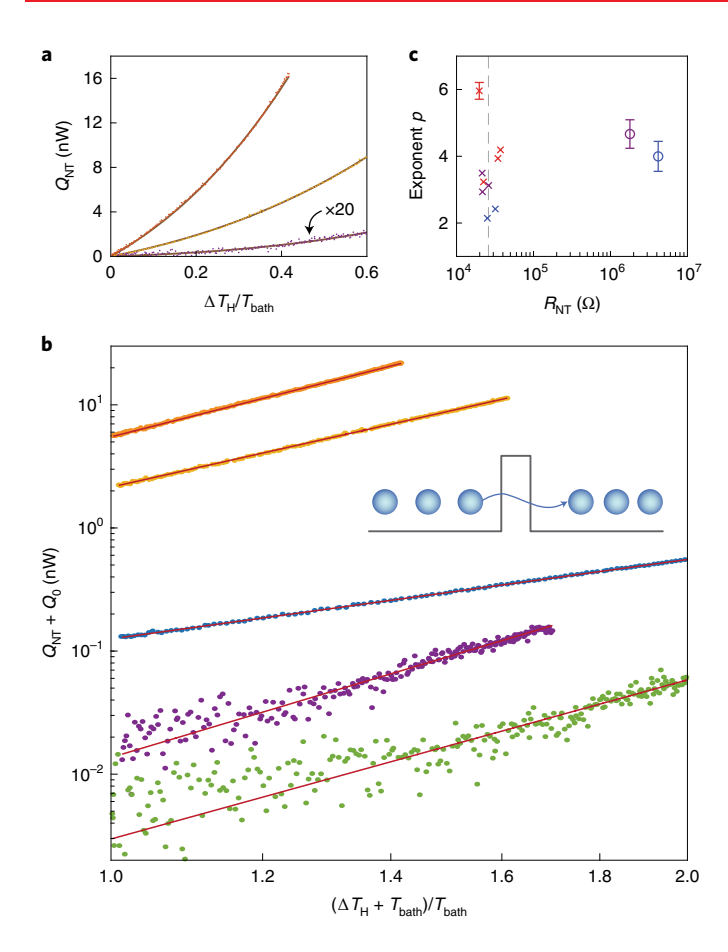


Fig. 4 | Nonlinear thermal transport in carbon NTs. a, Thermal current across the NT, $Q_{\rm NT}$, versus scaled thermal bias $\Delta T_{\rm H}/T_{\rm bath}$ for Device 1 at $T_{\rm bath}$ = 70 K and $V_{\rm g}^{\rm NT}$ = 0 (orange) and $T_{\rm bath}$ = 40 K and $V_{\rm g}^{\rm NT}$ = -10 V (yellow), and for Device 2 at $T_{\rm bath}$ = 50 K and $V_{\rm g}^{\rm NT}$ = -19.4 V (purple, multiplied by 20 to allow comparison). The brown lines represent fits to the plasmon hopping model (see main text). **b**, Log-log linearizing plot of NT thermal current versus thermal bias. The orange, yellow and purple datasets are identical to those defined in a. The blue and green datasets correspond to Device 1 with $T_{\rm bath}\!=\!6\,{\rm K}$ and $V_{\rm g}^{\rm NT}\!=\!$ –10 V, and Device 2 with $T_{\rm bath}\!=\!30\,{\rm K}$ and $V_{\alpha}^{NT} = -19.9 \text{ V}$, respectively. The red lines represent fits to the plasmon hopping model. The inset shows a schematic diagram of the plasmon hopping process, in which thermal electron density fluctuations are coupled across a barrier through long-range interactions, allowing the transport of energy even in an insulating system. c, Extracted exponents of the plasmon hopping model fit versus $R_{\rm NT}$ for Device 1 (crosses) at $T_{\rm bath}$ = 6 K (blue), 40 K (purple) and 70 K (red), and Device 2 (circles) at $T_{\text{bath}} = 30 \text{ K}$ (blue) and 50 K (purple). Symbols without error bars have statistical error less than the symbol size. The dashed vertical grey line corresponds to $R_{\rm NT} = h/e^2$.

accurate measurement of the transported energy, we had to ensure low electron energy loss to phonons in the thermometers. Graphene possesses several properties that are well-suited to electronic thermometry^{6,21,22,32}, including strong interactions, exceptionally low energy loss and small electronic thermal conductance (Methods). By defining local electrostatic gates for the hot and cold sides and exploiting tunable environmental disorder, graphene can be tuned to a diffusive regime, allowing for Joule heating and accurate noise thermometry on the hot and cold sides independent of the bridge state.

Electronic thermal transport in 2D graphene

As a first demonstration of electronic thermal transport measurement using non-local noise, we employed graphene as the bridge connecting graphene thermometers in a monolithic multi-terminal

graphene device. Figure 1d shows an H-shaped graphene device encapsulated in insulating hexagonal boron nitride (hBN). The device was etched to define the hot, cold and bridge regions. A low-frequency current was injected into the hot side, dissipating Joule power $P_{\rm H}$. As the power was increased, the measured noise power increased monotonically, resulting in a corresponding change in the measured temperature that was linear at low Joule power (Fig. 1d, left). For two different bridge electron densities, the hot side temperature change was effectively identical, indicating that only a small fraction of the total applied Joule power was transported across the bridge. The temperature change on the cold side (Fig. 1d, right), in contrast, was far smaller: for $\Delta T_{\rm H} = 0.6$ K, we observed $\Delta T_{\rm C} = 20-30$ mK, as expected for a small energy current across the bridge, and depended strongly on the bridge density.

Similar to the electrical conductance, the thermal conductance of the graphene bridge can be controlled by a voltage applied to a local gate. For this purpose, we fixed the applied power in the linear response regime and tuned the bridge electron density using a local metal gate on the bridge, $V_g^{\rm bridge}$ (Fig. 2a, inset). The hot and cold side gates were held fixed at values that maintained the thermometers in a diffusive regime. The hot side temperature change (Fig. 2a, top) was observed to be independent of the bridge density at three different bath temperatures. The cold side temperature change (Fig. 2a, bottom), in contrast, varied strongly as a function of the bridge gate, and showed a distinct trend that was reproduced at the three bath temperatures. Comparison with the four-point electrical resistance of the bridge (Fig. 2b, top) revealed that the Dirac peak of the graphene bridge, where resistance is maximal, corresponds to the minimum in ΔT_C , reflecting a thermal conductance modulation of the bridge with density.

To quantify the thermal conductance from the two measured temperatures, we require the energy current $Q_{\rm bridge}$. Because energy loss to phonons in the graphene cold side thermometer is negligible, it can be shown that

$$Q_{
m bridge} = rac{2}{3} G_{
m C}^{
m th} \Delta T_{
m C}$$
 ,

where $G_{\rm C}^{\rm th}$ is the thermal conductance of the cold side graphene measured by self-heating³⁶ (see Supplementary Section 4.2 for the derivation). Crucially, the cold side graphene serves both as a thermometer and a power meter. This can be understood by considering the effective thermal circuit of the device (Fig. 1b). In this model, $\Delta T_{\rm H,C}$ can be computed as a function of the total input power $Q_{\rm in}$ and the three thermal resistors, from which we obtain

$$G_{
m bridge}^{
m th} = G_{
m C'}^{
m th} \Delta T_{
m C'} / \left(\Delta T_{
m H'} - \Delta T_{
m C'}
ight)$$
 ,

showing that $Q_{\mathrm{bridge}} = G_{\mathrm{C'}}^{\mathrm{th}} \Delta T_{\mathrm{C'}}$ (the primed quantities refer to the circuit model; see Supplementary Section 5 for the connection between the thermal circuit and device). This result originates in the negligible energy loss to phonons. Thus, the temperature rise combined with the local thermal conductance accounts for all the power impinging on the cold side. This analysis can be extended to the case where electron-phonon coupling of the graphene thermometers is present, such as at high temperatures (T > 70 K), because the electron-phonon energy loss can be directly measured in the same set-up and accounted for quantitatively (Supplementary Section 6)^{6,21,22}. Here, we restricted ourselves to the low-temperature regime where electron-phonon coupling in the thermometers is negligible (see Supplementary Section 14 for an example at higher temperature where electron-phonon coupling is present). The resulting thermal conductance of the bridge exhibited a strong anticorrelation with the electrical resistance (Fig. 2b, middle). This observation can be made precise by computing a Lorenz ratio from the conductances, defined in analogy to the WF law as

NATURE NANOTECHNOLOGY ARTICLES

$$\frac{L}{L_0} = \frac{G^{\text{th}}R}{T_{\text{bath}}}/L_0$$
,

where $L_0 = \frac{\pi^2}{3} \left(\frac{k_{\rm B}}{e}\right)^2$ is the Lorenz number, where $k_{\rm B}$ is the Boltzmann constant and e is the electron charge. The Lorenz ratio at $T_{\rm bath} = 5$ K (Fig. 2b, bottom, blue curve) was close to 1 for the entire gate voltage range. This result demonstrates conclusively the thermal transport origin of the measured noise, validates the analysis methodology and indicates the negligible effect of phonons, radiation and contact resistance in this regime (Supplementary Sections 11 and 13).

At higher temperature, we found a density-dependent violation of the WF law, indicating the breakdown of a simple diffusive electronic system. At $T_{\rm bath}=20$ and 30 K, the Lorenz ratio was suppressed away from the Dirac point, exhibiting a local minimum and saturating at an intermediate value. Electron–electron interactions are predicted to suppress the Lorenz ratio away from charge neutrality^{37–43}. This is a sign of the onset of a hydrodynamic regime, recently discovered in graphene⁴⁴, in which electron–electron interactions scatter energy current while conserving charge current. Interactions combined with disorder lead to different signatures: with long-range disorder, the Lorenz ratio is suppressed at high density³⁹, whereas with short-range disorder it is suppressed in a lower density regime⁴⁰. The local minimum and high-density suppression of the Lorenz ratio thus point to a disordered hydrodynamic regime^{42,43}.

Thermal transport in 1D carbon nanotubes and Coulomb blockade

We now show that this method can be generalized to probe other low-dimensional materials. Graphene has previously been used as a contact intermediary for low-dimensional materials for which metallic contact is difficult to achieve⁴⁵⁻⁴⁸. By replacing the graphene bridge with a different material of interest, thermal contact may be established between the two graphene thermometers and a low-dimensional material bridge. To test this idea at its ultimate limit, we bridged two graphene thermometers with a carbon nanotube (NT), as shown in Fig. 3a (we consider an insulating, bulk material, RuCl₃, in Supplementary Section 14). Carbon NTs are one-dimensional metals or semiconductors, depending on their atomic structures⁴⁹. We grew carbon NTs, individually characterized them and incorporated them into graphene devices (Methods)^{50,51}. In these devices, the graphene thermometers were not covered with hBN to ensure electrical contact between the graphene and the NTs. As a result, the graphene thermometers were more disordered than fully encapsulated devices and experienced more energy loss at our operating temperatures (Supplementary Section 7). The thermal quantities presented here are thus lower bounds.

The electrical and thermal conductances, $G_{\rm NT}$ and $G_{\rm NT}^{\rm th}$, of a NT device (Device 1) were measured as a function of the voltage $V_{\rm g}^{\rm NT}$ applied to a local metal gate above the NT (Fig. 3b). At $T_{\rm bath} = 70~\rm K$, the electrical conductance exhibited a global minimum at $V_{\rm g}^{\rm NT} \approx 15~\rm V$, corresponding to a small gap in the electronic spectrum. The thermal conductance exhibited a similar feature. As the temperature was lowered, rapid modulations were observed in both the electrical and thermal conductance, becoming more pronounced at lower temperature. Throughout, we found that $G_{\rm NT}$ and $G_{\rm NT}^{\rm th}$ closely follow each other. The rapidly varying oscillatory conductance is indicative of the onset of Coulomb blockade through the disordered, substrate-supported NT⁵². For temperatures above the Coulomb blockade regime, the electrical conductance was nearly temperature-independent, evidencing the previously discovered weak electron—phonon interactions in carbon NTs (Supplementary Section 13). In a second device (Device 2) with a larger bandgap and higher channel resistance (Fig. 3c), the device is in a disordered

Coulomb blockade regime and exhibited sharper peaks alternating with vanishing electrical conductance at lower temperatures (Fig. 3c, bottom, inset). The thermal conductance trends with the electrical signal, despite the much higher channel resistance, greater than $1\,\mathrm{M}\Omega$, corresponding to $G_\mathrm{NT}\!\approx\!10^{-3}e^2/h$, where h is Planck's constant. The corresponding thermal measurement is accurate down to ~1% of the thermal conductance quantum $\frac{\pi^2}{h}\frac{k_\mathrm{B}}{h}T$ at 5 K (see Supplementary Section 12 for Device 1 data at 5 K). The measurement of electronic thermal transport in a system with far less than a single open quantum channel demonstrates the exceptional sensitivity of the graphene noise thermometers in our experiment.

The relation between $G_{\rm NT}$ and $G_{\rm NT}^{\rm th}$ can be described quantitatively by considering the Lorenz ratio

$$L_{\rm NT}/L_0 = G_{\rm NT}^{\rm th}/L_0 T G_{\rm NT},$$

For Device 1, with higher conductance, the Lorenz ratio was substantially above 1 for all the gate and temperature ranges measured (see lower panels of Fig. 3b), indicating a WF violation. This is consistent with previous measurements in quasi-1D systems and with several theoretical predictions^{2,53–55}. Close inspection revealed that $L_{\rm NT}/L_0$ exhibits peaks whenever the electrical conductance shows a dip, suggesting enhanced thermal conduction when electrical conduction is suppressed. In Device 2, with higher resistance, this enhanced thermal conduction is more clearly visible by plotting the inverse Lorenz ratio $(L_{NT}/L_0)^{-1}$, which is strongly positively correlated with the electrical conductance (Fig. 3c). This gate dependence rules out an extrinsic contact resistance as the source of the Lorenz ratio behaviour (Supplementary Section 11). The observed correlation of $(L_{\rm NT}/L_0)^{-1}$ with $G_{\rm NT}$ suggests the presence of a channel of excess thermal conduction that does not rely on direct electron transport.

One-dimensional plasmon hopping through long-range interactions

To account for a heat transport channel that is active even with suppressed electrical conduction, we propose here a model for plasmon hopping mediated by Coulomb interactions. The long-range Coulomb interaction has a measurable effect on many NT properties^{9,56,57}. We considered a minimal model of a 1D conductor separated into two parts by an impenetrable barrier. In the absence of electron transport, energy transport by hot electrons cannot be achieved. However, a long-range interaction allows for energy transfer across the barrier even in the absence of direct charge tunnelling. In this case, hot plasmons (density fluctuations) induce fluctuations across the electron barrier, leading to an energy current (Fig. 4b, inset). With Coulomb interactions, the plasmon hopping energy current obeys

$$Q \propto T_{
m H}^2 - T_{
m C}^2$$
,

while in the presence of screening by a nearby metal gate, the result is modified to $Q \propto T_{\rm H}^4 - T_{\rm C}^4$ (see Supplementary Section 8 for a detailed calculation).

We further tested long-range plasmonic energy transport in the NT devices by considering nonlinear thermal transport. We relaxed the condition $\Delta T_{\rm H} \lesssim T_{\rm bath}$ of the previous measurement by measuring the NT energy current $Q_{\rm NT}$ up to a large thermal bias $\Delta T_{\rm H}$. This measurement is the thermal analogue of a current–voltage curve in electrical measurements. Figure 4a shows $Q_{\rm NT}$ as a function of $\Delta T_{\rm H}/T_{\rm bath}$ at representative gate voltages for Devices 1 and 2, with $Q_{\rm NT}$ showing a superlinear increase for all measured gate voltages and bath temperatures. Figure 4b shows a log–log plot of $Q_{\rm NT}+Q_0$ versus $(\Delta T_{\rm H}+T_{\rm bath})/T_{\rm bath}$, where $Q_0=aT_{\rm bath}^p$ is a fitting parameter with a corresponding to the proportionality constant of the expression $Q_{\rm NT} \propto T_{\rm P}^p-T_{\rm C}^p$. The highly linear scaling observed suggests

that Q_{NT} follows the power law behaviour above with well-defined p. The slope of this plot provides p, which lies in the range 2–6, depending on the NT resistance $R_{\rm NT}$ (Fig. 4c). For the more resistive NT of Device 2, for which $R_{\rm NT} \gg h/e^2$, $p \approx 4$, suggesting that once the electron transmission coefficient is far less than 1 and tunnelling becomes suppressed, plasmon hopping through screened Coulomb interactions may make an important contribution to heat transport. For the highly conductive NT of Device 1, $R_{NT} \approx h/e^2$ and p ranges from 2 to 4. In this regime, electron transport is non-negligible, necessitating further theoretical modelling. We also note that our experimental observations cannot be described by an existing theory⁵⁸ in a disordered Luttinger regime with short-range interactions only, which predicts $Q \propto (T_{\rm H} - T_{\rm C})^{\frac{4}{3}}$ and gives p < 2. At a high conductance and high temperature point, we determined that $p \approx 6$, indicating the possible presence of additional energy transport mechanisms. The observed superlinear behaviour, and the associated exponents, are not explained by extrinsic effects such as contact resistance (see Supplementary Section 11, other parasitic contributions are ruled out in Supplementary Section 13). Our observations motivate future work to understand the interplay of long-range interactions and 1D electron and heat transport.

Conclusions

In conclusion, we have demonstrated the measurement of non-local voltage fluctuations induced by electronic thermal transport. Using graphene noise thermometers, we conducted a series of high-sensitivity electronic heat transport experiments in 2D van der Waals, 1D NTs and zero-dimensional localized systems, in which we observed interaction effects in energy transport. In addition, we have demonstrated thermal transport in a microscale bulk electrical insulator, RuCl₃, exhibiting measurable signals of magnetic thermal transport and a crossover to the phonon-coupled regime (Supplementary Section 14). Our approach enables the study of electronic thermal transport in a wide variety of low-dimensional systems that were previously out of reach.

Online content

Any methods, additional references, Nature Research reporting summaries, source data, extended data, supplementary information, acknowledgements, peer review information; details of author contributions and competing interests; and statements of data and code availability are available at https://doi.org/10.1038/s41565-021-01015-x.

Received: 3 March 2021; Accepted: 22 September 2021; Published online: 15 November 2021

References

- Franz, R. & Wiedemann, G. Ueber die Wärme-Leitungsfähigkeit der Metalle. Ann. Phys. 165, 497–531 (1853).
- Wakeham, N. et al. Gross violation of the Wiedemann–Franz law in a quasi-one-dimensional conductor. Nat. Commun. 2, 396 (2011).
- Smith, R. P. et al. Marginal breakdown of the Fermi-liquid state on the border of metallic ferromagnetism. *Nature* 455, 1220–1223 (2008).
- Tanatar, M. A., Paglione, J., Petrovic, C. & Taillefer, L. Anisotropic violation of the Wiedemann–Franz law at a quantum critical point. *Science* 316, 1320–1322 (2007).
- Hill, R. W., Proust, C., Taillefer, L., Fournier, P. & Greene, R. L. Breakdown of Fermi-liquid theory in a copper-oxide superconductor. *Nature* 414, 711–715 (2001).
- 6. Crossno, J. et al. Observation of the Dirac fluid and the breakdown of the Wiedemann–Franz law in graphene. *Science* 351, 1058–1061 (2016).
 7. Zhou, Y. et al. Bilayer Wigner crystals in a transition metal dichalcogenide
- heterostructure. *Nature* **595**, 48–52 (2021). 8. Smoleński, T. et al. Signatures of Wigner crystal of electrons in a monolayer
- Smoleński, T. et al. Signatures of Wigner crystal of electrons in a monolayer semiconductor. *Nature* 595, 53–57 (2021).
- 9. Shapir, I. et al. Imaging the electronic Wigner crystal in one dimension. *Science* **364**, 870–875 (2019).
- 10. Andrei, E. Y. & MacDonald, A. H. Graphene bilayers with a twist. *Nat. Mater.* **19**, 1265–1275 (2020).

- Mak, K. F., Shan, J. & Ralph, D. C. Probing and controlling magnetic states in 2D layered magnetic materials. *Nat. Rev. Phys.* 1, 646–661 (2019).
- 12. Li, M. & Chen, G. Thermal transport for probing quantum materials. MRS Bull. 45, 348–356 (2020).
- Tritt, T. M. Thermal Conductivity (Kluwer Academic and Plenum Press, 2004).
- Jezouin, S. et al. Quantum limit of heat flow across a single electronic channel. Science 342, 601–604 (2013).
- Banerjee, M. et al. Observed quantization of anyonic heat flow. Nature 545, 75–79 (2017).
- Banerjee, M. et al. Observation of half-integer thermal Hall conductance. Nature https://doi.org/10.1038/s41586-018-0184-1 (2018).
- Srivastav, S. K. et al. Universal quantized thermal conductance in graphene. Sci. Adv. 5, eaaw5798 (2019).
- Dutta, B. et al. Thermal conductance of a single-electron transistor. Phys. Rev. Lett. 119, 077701 (2017).
- Cui, L. et al. Quantized thermal transport in single-atom junctions. Science 355, 1192–1195 (2017).
- Mosso, N. et al. Heat transport through atomic contacts. *Nat. Nanotechnol.* 12, 430–433 (2017).
- Crossno, J., Liu, X., Ohki, T. A., Kim, P. & Fong, K. C. Development of high frequency and wide bandwidth Johnson noise thermometry. *Appl. Phys. Lett.* 106, 023121 (2015).
- Fong, K. C. et al. Measurement of the electronic thermal conductance channels and heat capacity of graphene at low temperature. *Phys. Rev. X* 3, 041008 (2013).
- Chiatti, O. et al. Quantum thermal conductance of electrons in a one-dimensional wire. *Phys. Rev. Lett.* 97, 056601 (2006).
- Molenkamp, L. W. et al. Peltier coefficient and thermal conductance of a quantum point contact. Phys. Rev. Lett. 68, 3765–3768 (1992).
- Seol, J. H. et al. Two-dimensional phonon transport in supported graphene. Science 328, 213–216 (2010).
- Kim, P., Shi, L., Majumdar, A. & McEuen, P. L. Thermal transport measurements of individual multiwalled nanotubes. *Phys. Rev. Lett.* 87, 215502 (2001).
- Mosso, N. et al. Thermal transport through single-molecule junctions. *Nano Lett.* 19, 7614–7622 (2019).
- 28. Cui, L. et al. Thermal conductance of single-molecule junctions. *Nature* **572**, 628–633 (2019).
- Johnson, J. B. Thermal agitation of electricity in conductors. Phys. Rev. 32, 97–109 (1928).
- Nyquist, H. Thermal agitation of electric charge in conductors. Phys. Rev. 32, 110–113 (1928).
- Qu, J. F. et al. Johnson noise thermometry. *Meas. Sci. Technol.* 30, 112001 (2019).
- 32. Fong, K. C. & Schwab, K. C. Ultrasensitive and wide-bandwidth thermal measurements of graphene at low temperatures. *Phys. Rev. X* 2, 031006 (2012).
- Yiğen, S. & Champagne, A. R. Wiedemann-franz relation and thermaltransistor effect in suspended graphene. Nano Lett. 14, 289–293 (2014).
- Sukhorukov, E. V. & Loss, D. Noise in multiterminal diffusive conductors: universality, nonlocality, and exchange effects. *Phys. Rev. B* 59, 13054–13066 (1999).
- Talanov, A. V., Waissman, J., Taniguchi, T., Watanabe, K. & Kim, P. High-bandwidth, variable-resistance differential noise thermometry. Rev. Sci. Instrum. 92, 014904 (2021).
- Pozderac, C. & Skinner, B. Relation between Johnson noise and heating power in a two-terminal conductor. *Phys. Rev. B* 104, L161403 (2021).
- Principi, A. & Vignale, G. Violation of the Wiedemann–Franz law in hydrodynamic electron liquids. *Phys. Rev. Lett.* 115, 056603 (2015).
- Lucas, A. & Das Sarma, S. Electronic hydrodynamics and the breakdown of the Wiedemann–Franz and Mott laws in interacting metals. *Phys. Rev. B* 97, 245128 (2018).
- Li, S., Levchenko, A. & Andreev, A. V. Hydrodynamic electron transport near charge neutrality. *Phys. Rev. B* 102, 075305 (2020).
- Xie, H.-Y. & Foster, M. S. Transport coefficients of graphene: interplay of impurity scattering, Coulomb interaction, and optical phonons. *Phys. Rev. B* 93, 195103 (2016).
- Lucas, A., Davison, R. A. & Sachdev, S. Hydrodynamic theory of thermoelectric transport and negative magnetoresistance in Weyl semimetals. *Proc. Natl Acad. Sci. USA* 113, 9463–9468 (2016).
- Zarenia, M., Principi, A. & Vignale, G. Disorder-enabled hydrodynamics of charge and heat transport in monolayer graphene. 2D Mater. 6, 035024 (2019).
- 43. Zarenia, M., Smith, T. B., Principi, A. & Vignale, G. Breakdown of the Wiedemann-Franz law in AB-stacked bilayer graphene. *Phys. Rev. B* **99**, 161407 (2019)
- 44. Lucas, A. & Fong, K. C. Hydrodynamics of electrons in graphene. *J. Phys. Condens. Matter* **30**, 53001 (2018).

NATURE NANOTECHNOLOGY ARTICLES

- 45. Cui, X. et al. Multi-terminal transport measurements of MoS₂ using a van der Waals heterostructure device platform. *Nat. Nanotechnol.* **10**, 534–540 (2015).
- 46. Liu, Y. et al. Toward barrier free contact to molybdenum disulfide using graphene electrodes. *Nano Lett.* **15**, 3030–3034 (2015).
- 47. El Abbassi, M. et al. Robust graphene-based molecular devices. *Nat. Nanotechnol.* **14**, 957–961 (2019).
- 48. Yang, C., Qin, A., Tang, B. Z. & Guo, X. Fabrication and functions of graphene-molecule-graphene single-molecule junctions. *J. Chem. Phys.* **152**, 120902 (2020).
- Ilani, S. & McEuen, P. L. Electron transport in carbon nanotubes. Annu. Rev. Condens. Matter Phys. 1, 1–25 (2010).
- Sfeir, M. Y. et al. Optical spectroscopy of individual single-walled carbon nanotubes of defined chiral structure. Science 312, 554–556 (2006).
- Cheng, A., Taniguchi, T., Watanabe, K., Kim, P. & Pillet, J. D. Guiding dirac fermions in graphene with a carbon nanotube. *Phys. Rev. Lett.* 123, 216804 (2019)
- 52. McEuen, P., Bockrath, M., Cobden, D., Yoon, Y.-G. & Louie, S. Disorder, pseudospins, and backscattering in carbon nanotubes. *Phys. Rev. Lett.* **83**, 5098–5101 (1999).

- Garg, A., Rasch, D., Shimshoni, E. & Rosch, A. Large violation of the Wiedemann-Franz Law in Luttinger liquids. *Phys. Rev. Lett.* 103, 096402 (2009).
- Kane, C. L. & Fisher, M. P. A. Thermal transport in a Luttinger liquid. *Phys. Rev. Lett.* 76, 3192–3195 (1996).
- Li, M.-R. & Orignac, E. Heat conduction and Wiedemann–Franz law in disordered Luttinger liquids. *Europhys. Lett.* 60, 432–438 (2002).
- Pecker, S. et al. Observation and spectroscopy of a two-electron Wigner molecule in an ultraclean carbon nanotube. *Nat. Phys.* 9, 576–581 (2013).
- Shi, Z. et al. Observation of a Luttinger-liquid plasmon in metallic single-walled carbon nanotubes. Nat. Photonics 9, 515–519 (2015).
- Fazio, R., Hekking, F. W. J. & Khmelnitskii, D. E. Anomalous thermal transport in quantum wires. *Phys. Rev. Lett.* 80, 5611–5614 (1998).

Publisher's note Springer Nature remains neutral with regard to jurisdictional claims in published maps and institutional affiliations.

© The Author(s), under exclusive licence to Springer Nature Limited 2021

Methods

Nanotube–graphene device fabrication. Carbon NTs were grown in a chemical vapour deposition (CVD) furnace following the method described previouslys The growth substrate consisted of a 5×5 mm² silicon chip with a slit in the centre, oriented perpendicular to the gas flow direction. Cobalt molybdenum catalyst was applied on one side of the slit, so that the NTs grew suspended across the slit. The suspended NTs were collected and characterized by Rayleigh scattering spectroscopy and imaging The chiral indices (and thus diameter and metallic/semi-conducting nature) of the NTs could be determined by matching the peaks in Rayleigh scattering intensity with NT optical transition energies.

Heterostructures of monolayer graphene on top of a 20–60 nm boron nitride flake were prepared using the inverted stacking technique. A 200–500-nm wide, >10-µm long slit was then created in the graphene by defining a poly(methyl methacrylate) (PMMA) mask using electron beam (e-beam) lithography and etching with O₂ plasma in a reactive ion etcher. A second e-beam lithography step defined a resist-free window above the heterostructure, while the rest of the chip remained coated in ~100 nm of resist. The chip and PMMA-coated sample were pressed together until mechanical contact was observed, then heated at 180 °C for 5 min to melt the resist. The chips were then cooled to 90 °C and slowly separated. Successful NT transfer was confirmed by electron microscopy or atomic force microscopy imaging.

Following NT transfer, electrical contacts were made at the edges of the graphene following the method reported previously 59 . The unwanted sections of the heterostructure were removed by reactive ion etching with CHF $_3$. An insulating layer of 120 nm SiO $_2$ was made above the NT by e-beam lithography of hydrogen silsesquioxane resist and development with CD-26 developer. A final e-beam lithography step defined the mask for the local top gate above the NT, which was formed by thermal evaporation of 3 nm Cr/7 nm Pd/70 nm Au (using an angled, rotating stage to mitigate height differences between different parts of the structure).

Differential noise thermometry with graphene. Each thermometer should measure the local hot and cold side temperatures $T_{\rm H}$ and $T_{\rm C}$ without cross-contamination of signals. Single-ended amplification of the hot and cold side noise power, S_H and S_C, would mix signals from either side due to a common ground and cause direct Joule heating of the cold side if the bridge were electrically conducting (Supplementary Section 3). We therefore implemented a differential noise thermometry measurement, described in detail elsewhere³⁵. Briefly, each terminal pair was connected to a balanced matching circuit that couples high-frequency signals into a differential low-noise amplifier (Fig. 1c). The resonant frequencies for the two matching circuits, between 100 MHz and 1 GHz, were chosen so as to have a frequency difference several times the circuit bandwidth, so that the hot and cold noise signals were mutually filtered and cross-correlations were suppressed. The amplified signals were bandpass-filtered and amplified at a second stage and sent through a power detector that generates a voltage proportional to the integrated high-frequency noise spectral density (Supplementary Section 10). By applying a low-frequency current at frequency f, the system was heated by Joule power at frequency 2f, and the output voltage was amplitude-modulated at frequency 2f. We isolated the change in noise power amplitude due to the applied Joule power using lock-in amplifiers. After calibration (Supplementary Section 1), the 2f noise power voltage signal was converted into a temperature rise, $\Delta T_{\rm H,C}$. Previously, we have shown this measurement can achieve sub-millikelvin precision in 30 s averaging time³⁵.

For thermal conductance measurement, the noise thermometer should have negligible energy loss. Graphene possesses a combination of properties that suit this purpose. Strong electron-electron interactions allow for thermalized temperature distributions down to sub-micrometre length scales^{60,61}. The light carbon lattice and stiff bonding result in weak electron-optical phonon coupling, while the large mismatch between the Fermi and sound velocities puts acoustic phonons in the quasi-elastic scattering regime in which energy loss is low⁶. The small Fermi surface around the Dirac point yields negligible Umklapp scattering, and the exceptional chemical cleanliness means inelastic impurity scattering

is largely absent. Because of its 2D nature, graphene possesses small electronic thermal conductance compared with three-dimensional bulk materials and is thus sensitive to small quantities of injected energy⁶²⁻⁶⁴.

Data availability

The data that support the findings of this study are available at the online depository Zenodo (https://doi.org/10.5281/zenodo.5500449).

References

- Wang, L. et al. One-dimensional electrical contact to a two-dimensional material. Science 342, 614–617 (2013).
- Müller, M., Schmalian, J. & Fritz, L. Graphene: a nearly perfect fluid. Phys. Rev. Lett. 103, 025301 (2009).
- Tielrooij, K. J. et al. Photoexcitation cascade and multiple hot-carrier generation in graphene. Nat. Phys. 9, 248–252 (2013).
- Walsh, E. D. et al. Graphene-based Josephson-junction single-photon detector. *Phys. Rev. Appl.* 8, 024022 (2017).
- Lee, G.-H. et al. Graphene-based Josephson junction microwave bolometer. Nature 586, 42–46 (2020).
- Kokkoniemi, R. et al. Bolometer operating at the threshold for circuit quantum electrodynamics. *Nature* 586, 47–51 (2020).

Acknowledgements

We thank B. Halperin, A. Lucas, S. D. Sarma, C. Mousatov, K. C. Fong and J. Crossno for helpful discussions, J. MacArthur for assistance with electronics design and construction, and M. Arino and H. Bartolomei for their assistance in the early stages of this work. This work was supported by ARO (W911NF-17-1-0574) for developing RF technology and characterization, and DOE (DE-SC0012260) for device fabrication and measurements. A.V.T. acknowledges support from the DoD through the NDSEG Fellowship Program. J.W. and P.K. acknowledge support from NSF (DMR-1922172) for data analysis. D.G.N. acknowledges support by the Office of Basic Energy Sciences of the DOE (DE-SC0017619). K.W. and T.T. acknowledge support from the Elemental Strategy Initiative conducted by the MEXT, Japan (grant number JPMXP0112101001), JSPS KAKENHI (grant number JP20H00354) and CREST (JPMJCR15F3), JST. Work by K.A.M. at the Argonne National Laboratory was supported by the DOE, Office of Science, Basic Energy Sciences, Materials Sciences and Engineering Division.

Author contributions

J.W. and P.K. conceived the experiments. J.W. performed the experiments and analysed the data. L.E.A. fabricated the NT–graphene devices. J.W., Y.J.S., and D.H.N. fabricated the graphene devices. M.R. fabricated the α -RuCl $_3$ devices. X.F. and D.G.N. synthesized the bulk α -RuCl $_3$ crystals. T.T. and K.W. synthesized the bulk hBN crystals. B.S. performed non-local noise calculations. K.A.M. developed the plasmon hopping theory. J.W., L.E.A., A.V.T., Z.Y., M.R., B.S., K.A.M. and P.K. discussed the results and interpretations. J.W. and P.K. wrote the manuscript in consultation with the other authors.

Competing interests

The authors declare no competing interests.

Additional information

 $\label{thm:contains} \textbf{Supplementary information} \ The online version contains supplementary material available at $$https://doi.org/10.1038/s41565-021-01015-x.$$

Correspondence and requests for materials should be addressed to Philip Kim.

Peer review information *Nature Nanotechnology* thanks Pramod Reddy and the other, anonymous, reviewer(s) for their contribution to the peer review of this work.

Reprints and permissions information is available at www.nature.com/reprints.